

Distribution System Blackstart and Restoration Using DERs and Dynamically Formed Microgrids

AQ1
AQ2

Salish Maharjan¹, Member, IEEE, Cong Bai², Graduate Student Member, IEEE, Han Wang³, Member, IEEE, Yiyun Yao⁴, Member, IEEE, Fei Ding⁵, Senior Member, IEEE, and Zhaoyu Wang⁶, Senior Member, IEEE

Abstract—Extreme weather events have led to long-duration outages in the distribution system (DS), necessitating novel approaches to blackstart and restore the system. Existing blackstart solutions utilize blackstart units to establish multiple microgrids (MGs), sequentially energize non-blackstart units, and restore loads. However, these approaches often result in isolated MGs. In DERs-aided blackstart, the continuous operation of these MGs is limited by the finite energy capacity of commonly used blackstart units like battery energy storage (BES)-based grid-forming inverters (GFMI). To address this issue, this article proposes a holistic blackstart and restoration framework that incorporates synchronization between dynamic MGs and the entire DS with the transmission grid (TG). To support synchronization, we leveraged virtual synchronous generator-based control for GFMI to estimate their frequency response to load pick-up events using only initial/final quasi-steady-state points. Subsequently, a synchronization switching condition is developed to model synchronizing switches, aligning them seamlessly with a linearized branch flow problem. Finally, we designed a bottom-up blackstart and restoration framework that considers the switching structure of the DS, energizing/synchronizing switches, DERs with grid-following inverters, and BES-based GFMI with frequency security constraints. The proposed framework is validated in IEEE-123-bus system, considering cases with two and four GFMI under various TG recovery instants.

Index Terms—Blackstart, cold load pick up, DigSILENT, microgrids, frequency security, restoration, resilience, synchronization, grid-forming inverters.

NOMENCLATURE

Abbreviations

CLPU	Cold load pick up
DS	Distribution system
GFMI, GFLI	Grid-forming/grid-following inverter
QSS	Quasi-steady-state

AQ3

Received 23 June 2024; revised 8 December 2024; accepted 25 January 2025. This work was supported in part by the National Renewable Energy Laboratory, operated by Alliance for Sustainable Energy, LLC, for the U.S. Department of Energy (DoE) under Contract DE-AC36-08GO28308; in part by the National Science Foundation through ECCS under Grant 2042314; in part by the Power System Engineering and Research Center (PSERC) under Grant S-110; and in part by the U.S. Department of Energy Solar Energy Technologies Office under Agreement 40385. Paper no. TSG-01101-2024. (Corresponding author: Zhaoyu Wang.)

Salish Maharjan, Cong Bai, Han Wang, and Zhaoyu Wang are with the Department of Electrical and Computer Engineering, Iowa State University, Ames, IA 50011 USA (e-mail: wzy@iastate.edu).

Yiyun Yao and Fei Ding are with the National Renewable Energy Laboratory, Golden, CO 80401 USA.

AQ4
AQ5

Color versions of one or more figures in this article are available at <https://doi.org/10.1109/TSG.2025.3536847>.

Digital Object Identifier 10.1109/TSG.2025.3536847

TG, MG	Transmission grid/Microgrid	35
<i>Parameters</i>		
$\alpha_1, \dots, \alpha_n$	Cold load pick up coefficients	37
\bar{P}^{DL}	Forecasted diversified load	38
\bar{P}^{PV}	Predicted PV generation	39
Δt	Time step	40
γ	Exponential constant term defined for GFMI	41
$[P^{PV}]$	Rated generation capacity of PV	42
$[f^{nad}]_-, [f^{nad}]_+$	Upper/lower limit of frequency nadir	44
$[f^{qss}]_-, [f^{qss}]_+$	Upper/lower limit of frequency at QSS	45
$[RoCoF]_-, [RoCoF]_+$	Upper/lower limit of RoCoF	46
θ_b^D	Power angle of the load	47
C	Battery capacity of BES-based GFMI	48
D	Damping constant of GFMI	49
f^*	Nominal frequency reference	50
H	Inertia constant of GFMI	51
K^f	Frequency droop of GFMI	52
M, ϵ	Big and small number	53
S^{rat}	Rating of GFMI	54
SS^{rat}	Capacity of sub station	55
t_o	Start time of blackstart	56
V^*	Nodal voltage reference	57

Indices and Sets

\mathcal{B}	Set of all buses	58
$\mathcal{B}(m)$	Set of buses contained by bus block m	59
\mathcal{B}_{CL}	Set of buses with non-switchable loads	60
\mathcal{B}_{NL}	Set of buses with switchable loads	61
\mathcal{B}_{PV}	Set of buses with PV	62
\mathcal{B}_{TG}	Set of buses where TG is interconnected	63
\mathcal{L}	Set of segments (e.g., lines and switches)	64
$\mathcal{L}(m)$	Set of segments contained by bus block m	65
\mathcal{L}^{ESW}	Set of energizing switches	66
\mathcal{L}^{WSW}	Set of synchronizing/smart switches	67
\mathcal{M}	Set of bus blocks	68
\mathcal{R}	Set of buses with GFMI	69
\mathcal{T}	Set of time step in the optimization problem	70
$\mathcal{W}(m)$	Set of switches surrounding bus block m	71
Φ	Set of phases	72
$N(j)$	Set of child buses of a bus j	73

Variables

P_j, Q_j	Vector of active/reactive power injection at bus j	74
------------	--	----

77	Φ_{ij}	Sub-matrix of v_i with elements corresponding to phase Φ_{ij}
78	$\Delta f_{i,t}$	Perturbation in nominal frequency of GFMI
79	Δv^{cc}	Incremental change in $(V^*)^2$ due to voltage droop
80	$\delta_{i,t}$	Binary variable defining synchronizing period
81	$\bar{R}_{ij}, \bar{X}_{ij}$	Balanced equivalent R/X matrices of unbalanced system
82		
83		
84	f	Frequency at QSS
85	f^{nad}	Frequency nadir
86	P^D	Active load demand
87	p^{ES}	output active power of BES-based GFMI
88	P^{PV}	Actual PV generation
89	P^{TG}, Q^{TG}	Active/reactive power from a TG
90	P_{ij}, Q_{ij}	Active/reactive power across a segment (i, j)
91	Q^D	Reactive load demand
92	q^{ES}	output reactive power from BES-based GFMI
93	Q^{PV}	Reactive power output of PV inverter
94	R	Number of root buses
95	$RoCoF$	Rate-of-change-of-frequency
96	SoC	State-of-charge of BES-based GFMI
97	v	Square of nodal voltage magnitude
98	y^B	Activation status of bus
99	y^L	Binary variable defining status of a line or a switch
100		
101	y^{BB}	Binary variable defining the status of bus block
102	y^D	Binary variable defining the status of load
103	$y_{b,t}$	Binary variable defining the status of TG
104	z^L	Binary variable defining the synchronizing instant

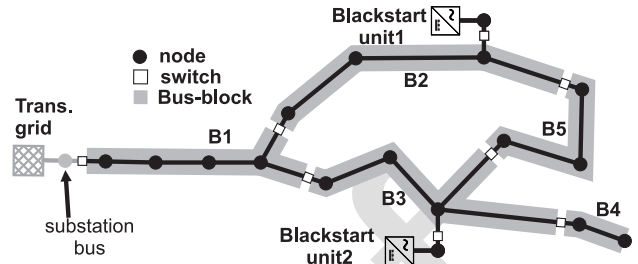


Fig. 1. Example DS illustrating bus-blocks, switches, and blackstart units.

Broadly, blackstart and load restoration strategies in the DS can be categorized into two main approaches, studied through: (a) determining the final configuration [4], [5], [6], and (b) sequencing configurations [7], [8], [9], [10], [11], [12], [13], [14], [15], [16]. The former works focus on establishing the final network topology without detailing the step-by-step evolution needed to achieve this configuration, which can complicate implementation. In contrast, the latter approach is more practical as it provides a sequence of feasible configurations to guide operators during the blackstart process. Furthermore, the latter works can be sub-classified into studies that either neglect [7], [8], [9], [10], [11], [12] or incorporate [13], [14], [15], [16] frequency constraints in their restoration models.

The authors in [7], [8] presented a detailed restoration model considering the distribution system's bus-block structures and connecting switches (as shown in Fig. 1). Furthermore, the authors in [9] enhanced the restoration model of DS accounting the flexibility of behind-the-meters DERs. Another enhancement of restoration model is presented in [10] by considering capabilities and operational limits of different switching devices of DS. In [11], the authors propose variable time step mixed-integer linear programming models to incorporate switches operating in multiple timescale while blackstarting DS. However, the models in [7], [8], [9], [10], [11] are designed for blackstart generators with a very large energy capacity (e.g., diesel or thermal generators) and loads without cold load pick-up (CLPU) effect. Considering blackstart units with finite energy capacity such as BES-based GFMI will potentially lead to different solutions and challenges, which were not studied in these above literature. The study in [12] incorporates GFMI/GFLI models in DS restoration and provides the percentage of load pick up schedules in each buses; however, this approach is not practical as most DS loads are not dispatchable. Moreover, all these works neglect frequency security constraints, which are crucial for ensuring the stability of MGs during blackstart operations.

A sequential restoration of loads in the DS, forming multiple dynamic MGs¹ (MGs) without exceeding maximum frequency nadir limits in each restoration sequence, is studied in [13]. This is one of the pioneering works where the frequency nadir limit is estimated without the need to simulate the dynamic model of the DS with blackstart generators. However, an

¹Unlike traditional MGs, which have a fixed configuration, dynamic MG can reconfigure themselves to optimize performance and enhance resilience [17].

I. INTRODUCTION

TRANSMISSION grids (TG) can be vulnerable to extreme weather events, which can result in blackouts in the downstream Distribution System (DS). Traditionally, distribution operators have relied on diesel generators (DGs) to blackstart and restore power during prolonged outages, ensuring a continuous power supply by maintaining a steady fuel source [1], [2]. With the anticipated widespread adoption of renewable energy sources in the DS, there is considerable interest in utilizing distributed energy resources (DERs) such as battery energy storage (BES) and renewables for blackstarting operations. Successfully implementing this technology would significantly reduce DS operators' reliance on DGs, which are known for their high operating costs.

DS utilities subscribe to weather forecasting agencies to predict extreme weather events, which aids in pre-event preparation where blackstart and load restoration plans are essential [3]. Blackstart planning with multiple BES inverters poses several challenges: (a) BES-based grid-forming inverters (GFMI) must operate within frequency security constraints, (b) their finite energy capacity must be optimally utilized to establish cranking paths for activating renewable-based grid-following inverters (GFLI) while supplying non-switchable loads, (c) optimizing synchronizing decisions to aggregate the energy and power capacity of BES-based GFMI for rapid load restoration, and (d) ensuring synchronization with the TG upon availability to maintain continuous operation.

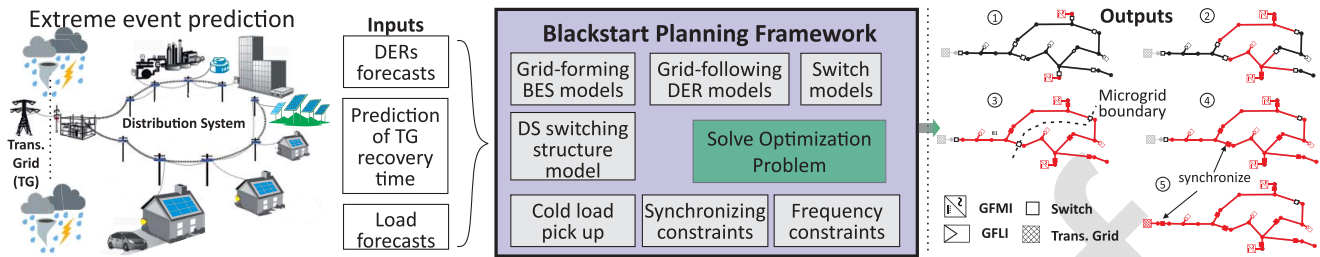


Fig. 2. Problem significance and overview of the proposed solution.

oversight of the work is that the microgrid also needs to satisfy the Rate-of-change-of-frequency(ROCOF) and quasi-steady-state (QSS) frequency limits not only the frequency nadir for secure operation [18]. A restoration model incorporating blackstart GFMI and non-blackstart GFLI with frequency dynamic constraints is developed in [14]. This model requires assistance from dynamic simulations to verify whether the frequency nadir exceeds secure limits when picking up loads. Although accurate, relying on simulations can be computationally expensive for large-scale restoration planning problems. The authors in [16] establish GFMI and GFLI models with a p-f droop-based relationship to estimate QSS frequency when restoring loads. However, frequency security constraints related to ROCOF and frequency nadir are ignored. All the above works neglect the synchronization between islands and with the transmission grid (TG), resulting in multiple islanded MGs forming at the end of the restoration process. However, the continuous operation of these MGs beyond the restoration period cannot be guaranteed if the blackstart units are battery energy storage (BES)-based and the non-blackstart units are renewable-based. To address this issue, synchronization must be an integral part of the restoration process, a consideration currently missing in the literature. Additionally, synchronization among islands facilitates resource sharing and enables a faster connection with the TG. The significance of synchronization for a resilient distribution system (DS) is advocated in [15], where the synchronization is conducted simply at the end of the restoration process. However, their work did not address synchronizing constraints and decisions within the blackstart problem itself.

Hence, this paper proposes a holistic bottom-up blackstart and load restoration planning framework leveraging BES-based GFMI and renewable GFLI. The proposed framework initiates blackstart with multiple GFMI, sequentially expands the boundaries of islanded MGs (referred to as dynamic MGs) while establishing cranking paths to GFLI, synchronizes MGs to form larger islands, and finally synchronizes with the TG to complete the restoration process. To incorporate synchronizing decisions in the problem, we first integrate virtual synchronous generator (VSG) control features into the GFMI. By leveraging VSG parameters (such as inertia constant and p-f droop), we establish and validate the GFMI's frequency response to cold load pick up (CLPU) in terms of quasi-steady-state frequency, ROCOF, and frequency nadir. This approach requires only the system's initial and final QSS points for frequency response estimation, making it

suitable for optimization problems and eliminating the need for dynamic simulation assistance. Additionally, we model GFMI frequency adjustment to facilitate synchronization. Secondly, we model synchronizing switches, establishing conditions for their operation that align with the branch flow model of the DS. A dynamic radiality constraint is designed to support synchronization by allowing GFMI to change the status of their root nodes to non-root nodes. Finally, all these models, along with GFLI dynamics, CLPU considerations, energizing switches, and the switching structure of the DS, are integrated with the linearized power flow model to develop a mixed-integer quadratic constrained problem for optimizing blackstart and load restoration. We validated the proposed framework using an unbalanced IEEE-123-bus system, considering cases with two and four GFMI under various scenarios of TG recovery instants.

To this end, the technical contributions of this work can be summarized as:

- Model a DERs-aided bottom-up blackstart framework that incorporates the frequency response of VSG-based GFMI. Validate the GFMI's estimated frequency response to load pick-up events by using a dynamic model of the DS and GFMI.
- Model synchronizing switches (SSWs) with conditions that align with the branch flow-based restoration model. Optimize both the energizing and synchronizing switches efficiently in the blackstart and restoration process.
- Develop dynamic radiality constraints to support synchronization and allow dynamic MGs to expand and integrate their boundaries during blackstart process.

The remainder of the paper is organized as follows: Section II provides an overview of the problem and the proposed solution. Sections III and IV present detailed models of DS components and describe the bottom-up blackstart and load restoration framework, with a focus on GFMI frequency dynamics and synchronization constraints. Section V discusses the simulation results of the proposed framework, considering multiple GFMI. Finally, Section VI concludes the paper.

II. OVERVIEW OF THE PROBLEM AND THE PROPOSED SOLUTION

Utilities routinely monitor weather forecasts to anticipate extreme weather events and enhance disaster preparedness. For instance, U.S. utilities typically implement storm preparation plans [19]. When a day-ahead forecast predicts severe weather,

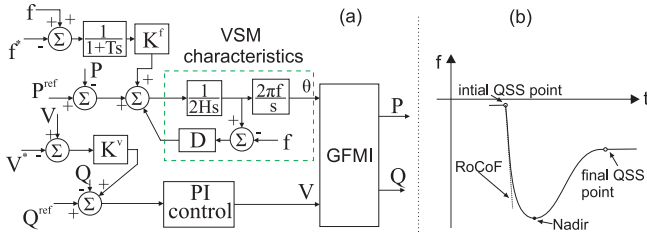


Fig. 3. (a) Control diagram and (b) dynamic frequency response of a VSG.

an emergency response is triggered, prompting utilities to plan for blackstart and load restoration. These plans provide a preliminary roadmap for post-event recovery efforts. Traditionally, blackstart strategies have relied on straightforward measures, such as maintaining diesel reserves and utilizing utility-owned diesel plants to restore loads. However, these conventional methods often involve intentional temporary blackouts during reconnection with the TG, adversely affecting system reliability and resilience.

The integration of DERs, intelligent electronic devices like synchronizing or smart switches, and advanced communication and sensor networks in DS has opened new avenues for optimizing blackstart procedures. These advancements can significantly improve reliability and resilience. However, effective blackstart planning with DERs requires addressing challenges such as their variability, limited energy storage, inverter control technologies (e.g., GFM and GFL), and frequency security constraints. Synchronization strategies are also critical for seamless reconnection with the TG. To tackle these challenges, we propose a dynamic MG-based blackstart planning framework, as illustrated in Fig. 2. Key inputs include forecasts for DER generation, TG recovery time, and load demands. The framework outputs a sequence of feasible configuration of dynamic MGs due to switching actions, encompassing both energizing and synchronizing steps, guiding the system from blackstart initiation to the complete restoration of loads.

III. MODELING DISTRIBUTION SYSTEM AND ITS COMPONENTS CONSIDERING SYNCHRONIZATION

In this section, we model DS components—such as GFMI, GFLI, and loads—considering their roles in synchronizing GFMI when interconnecting two MGs or connecting to the TG. Additionally, we describe the switching structure of the DS, which involves two types of switches: energizing and synchronizing. We also outline the relationships between the active and inactive states of bus blocks, lines, buses, and switches. Finally, we present a linear power flow model of DS considering the switching structure.

A. Modeling BES-Based Grid-Forming Inverter (GFMI)

We consider all GFMI to be 3- ϕ Virtual Synchronous Generator (VSG) designed with inertia constant (H) and damping constant (D) to emulate the synchronous generator's characteristics. A VSG operates with a voltage-frequency ($V-f$) control mode with a suitable frequency and voltage

droops for active and reactive power sharing between other VSGs [20].

At normal operating conditions, GFMI regulates its terminal voltage and frequency close to nominal values, allowing them to change with respect to voltage and frequency droop gains (K^v and K^f), as shown in Fig. 3a. To comply with the branch-flow model of the distribution system, we will refer to the square of voltage magnitude ($v = |V|^2$) as the control variable for GFMI. Hence, the voltage and frequency at QSS are defined for all GFMI buses in \mathcal{R} as:

$$v_{i,n,t} = (V^*)^2 + \Delta v_{i,t}^{cc} \quad \forall i \in \mathcal{R}, n \in \Phi, \quad (1)$$

$$f_{i,t} = f^* \left(1 - \frac{\sum_{n \in \Phi} p_{i,n,t}^{ES}}{S_i^{rat} (D_i + K_i^f)} \right) \quad \forall i \in \mathcal{R}. \quad (2)$$

Here, Φ is a set of phases in bus i . V^* and Δv^{cc} are a nominal voltage reference and incremental voltage appearing due to the voltage droop. The derivation of (1) is discussed in Appendix A. Furthermore, (2) is defined in [21], where f^* is the nominal frequency set-point, p^{ES} is the output active power, and S^{rat} is the rated capacity of the inverter. GFMI has operational constraints over voltage, frequency, and power output, and are defined as:

$$(0.95V^*)^2 \leq v_{i,n,t} \leq (1.05V^*)^2, \quad \forall i \in \mathcal{R}, n \in \Phi \quad (3)$$

$$[f^{qss}] \leq f_{i,t} \leq [f^{qss}], \quad \forall i \in \mathcal{R} \quad (4)$$

$$\max_{n \in \Phi} \{ (p_{i,n,t}^{ES})^2 + (q_{i,n,t}^{ES})^2 \} \leq \left(\frac{1}{3} S_i^{rat} \right)^2 \quad \forall i \in \mathcal{R} \quad (5)$$

Here, $[f^{qss}]$ and $[f^{qss}]$ are upper and lower boundaries of the frequency at quasi-steady-state. The thermal limit of GFMI (5) has been adopted from [22], where q^{ES} refers to reactive power at each phase. Constraint (5) signifies that once any phase of a GFMI reaches its thermal limit (i.e., $\frac{1}{3} S_i^{rat}$), the remaining two phases cannot be further loaded. BES-based GFMI will have an additional constraint on the state of charge (SoC), which is expressed as:

$$SoC_{i,t} = SoC_{i,t-1} + \frac{1}{C_i} \sum_{n \in \Phi} \{ \Delta p_{i,n,t}^{ES} \} \Delta t, \quad \forall i \in \mathcal{R} \quad (6)$$

$$\text{where, } \Delta p_{i,n,t}^{ES} = p_{i,n,t}^{ES} - p_{i,n,t-1}^{ES}$$

Note that charging and discharging efficiencies are neglected in (6) as the main focus during blackstart is to restore the loads more efficiently than considering the battery losses. C_i and Δt are battery capacity and a time-step, respectively.

1) *Constraining Dynamic Frequency Responses to Comply With Security Limits:* When a GFMI picks up loads, the frequency initially declines abruptly during the first few seconds. After this initial drop, the frequency is regulated by droop control to bring it back within the QSS limits. This dynamic frequency response between the initial and final QSS points is shown in Fig. 3b. GFMI is required to comply its dynamic frequency response in terms of $RoCoF$ and frequency-nadir (f^{nad}) for secure operation defined by NERC [18]. We leverage the work in [21] to estimate $RoCoF$

357 and f^{nad} of VSG based on initial and final QSS operating points
 358 as:

$$359 \quad RoCoF_{i,t} = \frac{\sum_{n \in \Phi} \Delta P_{i,n,t}^{ES}}{2S_i^{rat} H_i} \quad (7)$$

$$360 \quad f_{i,t}^{nad} = \left[f_{i,t} - f^* \frac{\sum_{n \in \Phi} \Delta P_{i,n,t}^{ES}}{S_i^{rat} (D_i + K_i^f)} (1 + \gamma_i) \right] \quad (8)$$

361 Detailed calculation of γ for VSGs is discussed in
 362 Appendix B. Note that RoCoF and f^{nad} for each VSG depend
 363 on its active power output either when operating autonomously
 364 or in parallel. Finally, we impose a security constraint on the
 365 dynamic frequency responses as:

$$366 \quad [RoCoF] \leq RoCoF_{i,t} \leq [RoCoF] \quad \forall i \in \mathcal{R}, \quad (9)$$

$$367 \quad [f^{nad}] \leq f_{i,t}^{nad} \leq [f^{nad}] \quad \forall i \in \mathcal{R}. \quad (10)$$

368 Note that equations (2), (7), and (8) represent dynamic
 369 frequency responses derived for synchronous generators
 370 in [21]. We have verified that they also apply for VSG-based
 371 GFMI through dynamic simulations in DigSilent Power
 372 Factory in Section V-A. A blackstart problem accounting for
 373 these dynamic frequency responses of GFMI, without the
 374 assistance from computational expensive dynamic simulation,
 375 are our contribution of this paper.

376 B. Modeling Synchronization of GFMI

377 GFMI needs to adapt its frequency set-points to allow
 378 synchronization with other GFMI or the TG [23]. This is
 379 achieved by allowing perturbation in frequency (Δf^*) of
 380 GFMI while performing synchronization. Hence, (2) is defined
 381 with synchronizing decisions as:

$$382 \quad f_{i,t} = f^* \left(1 - \frac{\sum_{n \in \Phi} P_{i,n,t}^{ES}}{S_i^{rat} (D_i + K_i^f)} \right) + \delta_{i,t} \Delta f_{i,t}^*. \quad (11)$$

383 Here, δ is a binary variable that is set to 1 only during the
 384 synchronizing period. Equation (11) allows frequency pertur-
 385 bation in a GFMI attempting to synchronize, while keeping the
 386 frequencies of other GFMI intact. This is like master-slave
 387 synchronization approach which can be more restrictive [24].
 388 Hence, we implement co-operative synchronization approach,
 389 where all GFMI decide the suitable synchronizing frequency,
 390 as:

$$391 \quad f_{i,t} = f^* \left(1 - \frac{\sum_{n \in \Phi} P_{i,n,t}^{ES}}{S_i^{rat} (D_i + K_i^f)} \right) + \left(\sum_{b \in \mathcal{R}} \delta_{b,t} \right) \Delta f_{i,t}^*. \quad (12)$$

392 The δ is interlinked with the network radiality constraint
 393 defined in Section IV-A. Note that the bilinear terms
 394 in (11) and (12) can be relaxed into linear constraints
 395 using McCormick relaxation [25], and is further illustrated in
 396 Appendix C.

397 C. Modeling Grid-Following PV Inverters

398 All 3- ϕ and 1- ϕ PV inverters are operated in grid-following
 399 mode, meaning they can come online only after the bus they
 400 are connected to is energized. If $y_{b,t}^B, b \in \mathcal{B}_{PV}$ are binary

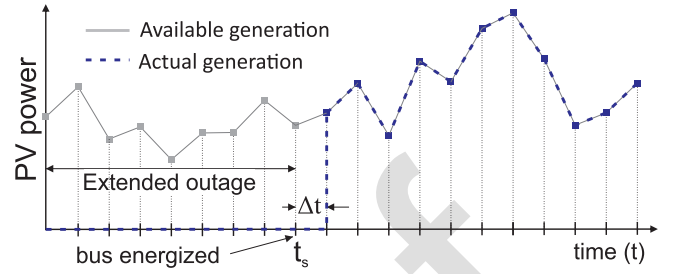


Fig. 4. Energization of grid-following DERs such as PV.

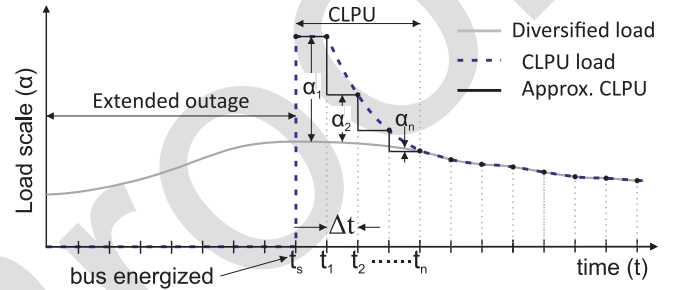


Fig. 5. Cold load pickup model after an extended outage.

401 variables representing the energization status of buses where
 402 PVs are connected, then the grid-following nature of PV
 403 inverters can be modeled as:

$$404 \quad P_{b,t}^{PV} = \bar{P}_{b,t}^{PV} y_{b,t-1}^B \quad \forall b \in \mathcal{B}_{PV} \quad (13)$$

405 Here, $P_{b,t}^{PV}$ and $\bar{P}_{b,t}^{PV}$ are actual and predicted PV power
 406 generation. Note that we multiply PV generation in (13) by
 407 $y_{b,t-1}^B$ rather than $y_{b,t}^B$ due to consideration of an intentional
 408 time delay of one-time step. The typical inverter intentional
 409 time delay of grid-following renewable generation is 2-15
 410 minutes, as recommended by IEEE 1547-2018. The impact of
 411 intentional time delay in the output PV power is illustrated
 412 in Fig. 4. The reactive power injections are assumed to be
 413 controllable, and their capabilities are defined to follow IEEE
 414 1547-2018 standards in [26] as:

$$415 \quad -0.484 [P_b^{PV}] y_{b,t-1}^B \leq Q_{b,t}^{PV} \leq 0.484 [P_b^{PV}] y_{b,t-1}^B. \quad (14)$$

416 Here, $[P]_b^{PV}$ is the rated generation capacity of PV located at
 417 bus b .

418 D. Modeling Cold Load Pick Up (CLPU)

419 Black starting a distribution system requires picking up cold
 420 loads, leading to initial higher power demand compared to
 421 its diversified form. The initial elevated demand gradually
 422 decreases with time in a non-linear way and finally follows the
 423 diversified demand, as illustrated in Fig. 5. This phenomenon
 424 is called the CLPU effect [27].

425 In this work, to eliminate the non-linearity introduced by the
 426 CLPU effect, a staircase modeling approach is developed, as
 427 shown in Fig. 5. The developed approach captures the CLPU
 428 effect by introducing CLPU coefficients $\{\alpha_1, \alpha_2, \dots, \alpha_n\}$,
 429 which progressively diminishes over time. Actual demand is
 430 then modeled as the product of their diversified load and the
 431 respective coefficient.

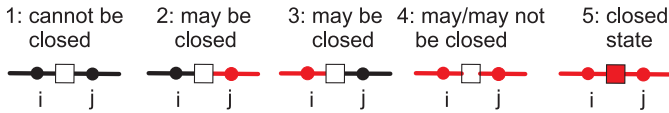


Fig. 6. Possible switch states while blackstarting.

Generally, a distribution system has many hard-wired loads and few switchable loads. Hard-wired loads are non-switchable and are picked up upon energization of the bus to which they are connected. In contrast, switchable loads can be picked up in a controlled way. We assume switchable and non-switchable loads do not co-exist in the same bus for brevity. We represent buses containing switchable load by \mathcal{B}_{CL} and non-switchable load by \mathcal{B}_{NL} , and assume $\mathcal{B}_{CL} \cap \mathcal{B}_{NL} = \{\}$. Depending upon the status of the load $y_{b,t}^D$, the power demand of the switchable or non-switchable loads can be defined as:

$$P_{b,t}^D = \bar{P}_{b,t}^{DL} \left(\alpha_1 (y_{b,t}^D - y_{b,t-1}^D) + \alpha_2 (y_{b,t-1}^D - y_{b,t-2}^D) + \alpha_3 (y_{b,t-2}^D - y_{b,t-3}^D) + y_{b,t}^D \right) \quad \forall b \in \mathcal{B}_{CL} \cup \mathcal{B}_{NL}, \quad (15)$$

$$Q_{b,t}^D = P_{b,t}^D \tan(\theta_b^D) \quad \forall b \in \mathcal{B}_{CL} \cup \mathcal{B}_{NL}. \quad (16)$$

Here, $\bar{P}_{b,t}^{DL}$ is forecasted diversified load. The terms within the bracket in (15) define the approximated CPU effect. If the load at bus b is non-switchable, then both the bus and load will have the same status, which is defined as:

$$y_{b,t}^D = y_{b,t}^B \quad \forall b \in \mathcal{B}_{NL} \quad (17)$$

E. Modeling Switching Structure of Distribution System

A distribution system comprises a cluster of buses, referred to as bus-block [14], that are interconnected by switches, as shown in Fig. 1. During a blackstart, these bus blocks are energized sequentially with the help of blackstart resources by closing the switches one after another. It is essential to model the switching constraints to generate technically feasible switching sequences, as discussed below.

1) *Modeling Switches*: To integrate with the power flow model in Section III-F, we will represent all the switches by a negligible-impedance line (i, j) where $i, j \in \mathcal{B}$. A switch may be in five states, shown in Fig. 6, while black-starting the system. In state 1, switching is infeasible because a switch requires cranking power to operate remotely. Switching is feasible at states 2 and 3 while switching at state 4 depends on the switch's capability. Only a switch with synchronizing capability can turn ON at state 4. Hence, we will consider two types of switches: (a) energizing switches (ESW) and (b) synchronizing switches (SSW), and model their switching constraints. The switching constraints at all five states are shown in Table I for both the ESW and SSW, where $\Delta y_{ij,t}^L = y_{ij,t}^L - y_{ij,t-1}^L$.

a) *Energizing switch (ESW)*: Energizing switches (e.g., breakers, reclosers, or tie-switches) are turned ON to power the inactive portion of the DS. However, they cannot close the switch to connect two active buses, as these may have different phases and frequencies. We define the set of all ESW

TABLE I
CONSTRAINTS FOR ENERGIZING AND SYNCHRONIZING SWITCHES (i, j)

state	$y_{i,t-1}^B$	$y_{j,t-1}^B$	$y_{ij,t-1}^L$	$\Delta y_{ij,t}^L$ constraints	
				ESW	SSW
1	0	0	0	$\Delta y_{ij,t}^L = 0$	
2	0	1	0	$\Delta y_{ij,t}^L \leq 1$	
3	1	0	0	$\Delta y_{ij,t}^L \leq 1$	
4	1	1	0	$\Delta y_{ij,t}^L = 0$	$\Delta y_{ij,t}^L \leq 1$
5	1	1	1	$\Delta y_{ij,t}^L = 0$	

by \mathcal{L}^{ESW} . All the constraints for every state of ESW in Table I can be succinctly defined for all $(i, j) \in \mathcal{L}^{ESW}$ as:

$$y_{ij,t}^L \leq y_{i,t-1}^B + y_{j,t-1}^B \quad (18)$$

$$\Delta y_{ij,t}^L \leq 2 - y_{i,t-1}^B - y_{j,t-1}^B, \quad \Delta y_{ij,t}^L \geq 0 \quad (19)$$

b) *Synchronizing switch (SSW)*: Synchronizing switches are special switches equipped with Intelligent Electronic Devices (IEDs) with the additional functionality of monitoring voltages across the switch at a fast rate to facilitate synchronization of the grids. They are also referred to as smart switches in [15]. We represent all SSWs by a set \mathcal{L}^{SSW} . Similar to ESW, switching constraints for all $(i, j) \in \mathcal{L}^{SSW}$ can be defined as:

$$y_{ij,t}^L \leq y_{i,t-1}^B + y_{j,t-1}^B, \quad \Delta y_{ij,t}^L \geq 0 \quad (20)$$

To close an SSW, it is significant to match the voltage and angle of buses i and j to ensure secure connection of grids. Imposing this constraint is challenging when using the branch-flow model (outlined in Section III-F), as it does not use node voltages in polar form. However, we can satisfy this constraint by ensuring negligible (ideally zero) power flow across the SSW when it is switched ON and then relaxing the power flow afterward (More thoroughly discussed in Appendix D). This will require identifying the instant of closing SSW. We know when SSW is switched ON, $\Delta y_{ij,t}^L \rightarrow 1$. However, this is not sufficient as this condition is true even for a ESW. Additionally, when SSW is switched ON, the condition $(y_{i,t-1}^B + y_{j,t-1}^B - y_{ij,t}^L) \rightarrow 1$, which does not hold for ESWs. Hence, the synchronizing instant can be defined by the multiplication of two conditions, as:

$$z_{ij,t}^L = \Delta y_{ij,t}^L (y_{i,t-1}^B + y_{j,t-1}^B - y_{ij,t}^L) \quad (21)$$

Note that (21) is a bilinear constraint involving three bilinear terms. Although it is non-convex, it can be reformulated into a set of linear constraints using McCormick relaxation, as illustrated in Appendix C. Utilizing $z_{ij,t}^L$, the synchronizing constraint can be defined for all $(i, j) \in \mathcal{L}^{SSW}$ as:

$$-\left(1 - z_{ij,t}^L\right)M - \epsilon \leq P_{ij,t} \leq \epsilon + \left(1 - z_{ij,t}^L\right)M \quad (22)$$

$$-\left(1 - z_{ij,t}^L\right)M - \epsilon \leq Q_{ij,t} \leq \epsilon + \left(1 - z_{ij,t}^L\right)M \quad (23)$$

Here, M and ϵ are big and small numbers.

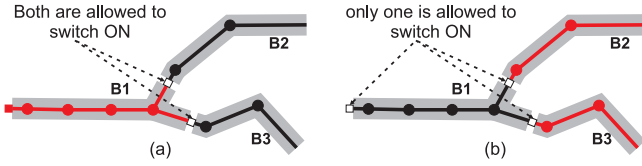


Fig. 7. (a) Multiple switches associated with active bus block (e.g., B1) can be switched ON. (b) Only one switch associated with inactive bus block (e.g., B1) can be switched ON.

When an ESW or a SSW (i, j) is closed, the frequencies at buses i and j should follow or match respectively. This constraint can be defined for all $(i, j) \in \mathcal{L}^{ESW} \cup \mathcal{L}^{SSW}$ as:

$$-\left(1 - y_{ij,t}^L\right)M - \epsilon \leq f_{i,t} - f_{j,t} \leq \epsilon + \left(1 - y_{ij,t}^L\right)M \quad (24)$$

SSW with synchronizing constraints are the novel contribution of this paper, which are integral for modeling synchronizing dynamic MGs. This model can be seamlessly integrated with linear power flow model of DS, by considering these switches as a line with very small impedance.

2) *Bus Blocks Energizing Constraints:* In a multi-configurable distribution system, a bus block is segregated by multiple switches (for reference, see Fig. 1) and, hence, can be energized by closing any of them. Additionally, once a bus block is energized, it is not de-energized. We represent a set of bus blocks of DS by \mathcal{M} and the switches associated with each bus block $m(m \in \mathcal{M})$ by a set $\mathcal{W}(m)$. Hence, the energizing constraints of a bus block are modeled as follows.

$$y_{m,t}^{BB} \geq y_{ij,t}^L \quad \forall \{m \in \mathcal{M} | (i, j) \in \mathcal{W}(m)\} \quad (25)$$

$$y_{m,t}^{BB} \geq y_{m,t-1}^{BB} \quad (26)$$

Here, $y_{m,t}^{BB}$ is a binary variable representing its activation status. Furthermore, an energizing of bus block will activate its lines and buses, which is modeled as:

$$y_{ij,t}^L = y_{m,t}^{BB} \quad \forall \{m \in \mathcal{M} | (i, j) \in \mathcal{L}(m)\} \quad (27)$$

$$y_{i,t}^B = y_{m,t}^{BB} \quad \forall \{m \in \mathcal{M} | i \in \mathcal{B}(m)\} \quad (28)$$

Here, $\mathcal{L}(m)$ and $\mathcal{B}(m)$ represent the set of lines and buses associated with bus block m . To ensure the feasibility of switching, we allow multiple switches associated with an active bus block to be turned ON, but only one switch for an inactive bus block (illustrated in Fig. 7). An inactive bus block is limited to only one switch to prevent energization from multiple active bus blocks, which may belong to different MGs where synchronization will be necessary before merging them. This constraint is illustrated in Fig. 7(b) and can be define as:

$$\sum_{(i,j) \in \mathcal{W}(m)} y_{ij,t}^L - \sum_{(i,j) \in \mathcal{W}(m)} y_{ij,t-1}^L \leq M y_{m,t}^{BB} + 1 \quad \forall m \in \mathcal{M} \quad (29)$$

Furthermore, the frequency measured at any bus within the bus block should have same value. This can be achieved with the help of following constraint defined for each segment m .

$$f_{b,t} = f_{m,t} \quad \forall b \in \mathcal{M}(m) \quad (30)$$

F. Linear Power Flow Model Adaptive to Network Topology

The study conducted in [28] investigated a linearized power flow model for an unbalanced distribution system with all active lines and buses. However, the number of active lines and buses are changing while blackstarting. To adapt with active/inactive elements, we relax the power flow equations in [28] with the help of binary variables representing the active/inactive status of the lines (y_{ij}^L) and buses (y_i^B). We establish a power flow model by defining voltage equations for all lines (i.e., $\forall (i, j) \in \mathcal{L}$) as:

$$v_{j,t} \leq v_{i,t}^{\Phi_{ij}} - 2(\bar{R}_{ij}P_{ij,t} + \bar{X}_{ij}Q_{ij,t}) + M^{\Phi_{ij}}(1 - y_{ij,t}^L) \quad (31a)$$

$$v_{j,t} \geq v_{i,t}^{\Phi_{ij}} - 2(\bar{R}_{ij}P_{ij,t} + \bar{X}_{ij}Q_{ij,t}) - M^{\Phi_{ij}}(1 - y_{ij,t}^L) \quad (31b)$$

$$-M^{\Phi_{ij}}y_{ij,t}^L \leq P_{ij,t} \leq M^{\Phi_{ij}}y_{ij,t}^L \quad (31c)$$

$$-M^{\Phi_{ij}}y_{ij,t}^L \leq Q_{ij,t} \leq M^{\Phi_{ij}}y_{ij,t}^L \quad (31d)$$

$$0.9025^{\Phi_{ij}}y_{j,t}^B \leq v_{j,t} \leq 1.1025^{\Phi_{ij}}y_{j,t}^B \quad (31e)$$

Here, $v_{j,t}$ is a vector representing the square of voltage magnitude at each phase in the bus j ; $v_{i,t}^{\Phi_{ij}}$ is sub-matrix of $v_{i,t}$ containing the entries associated with Φ_{ij} ; P_{ij} and Q_{ij} are real and reactive power flow on line (i, j) ; M is a user-defined large constant vector that helps to relax the power flow constraints (31a)-(31b) even when the line (i, j) is unenergized (i.e., when $y_{ij,t}^L \rightarrow 0$). A multi-configurable distribution system is an undirected graph, particularly while black-starting, without prior information of parent-child relationships among its buses. Nonetheless, the relaxation in (31c)-(31d) allows bidirectional power flow, allowing us to initially treat it as a directed graph with assumed parent-child relationships. Finally, (31e) is a box constraint for $v_{i,t}$ to regulate voltage magnitude between 0.95 to 1.05 p.u. if the status of the bus is active (i.e., when $y_i^B \rightarrow 1$), otherwise squeezed to 0. \bar{R}_{ij} and \bar{X}_{ij} are matrix parameters associated with line resistance and reactance, whose computations are shown in [28].

Neglecting the line losses, the power flow on line (i, j) is written for all $(i, j) \in \mathcal{L}$ as:

$$P_{ij,t} = \sum_{k \in N(j)} P_{jk,t} - p_{j,t} \quad (32a)$$

$$Q_{ij,t} = \sum_{k \in N(j)} Q_{jk,t} - q_{j,t} \quad (32b)$$

Here, $N(j)$ is a set child bus of bus j ; p_j/q_j is a vector of net active/reactive power injection at bus j such that generation is assumed positive and demand is negative.

G. Modeling Transmission Grid Outage and Recovery

A DS is disconnected from out-of-service TG during the blackstart and later reconnected when the TG is restored. We represent a set of transmission-distribution interconnection bus as \mathcal{B}^{TG} and its active/inactive status by a binary parameter $y_{b,t}^{TG}$. Note that $y_{b,t}^{TG}$ is an input parameter, whose value is set to 0 when the TG is out-of-service and 1 when it is active. Hence, the TG is modeled for all $b \in \mathcal{B}^{TG}$ as:

$$\left(P_{b,t}^{TG}\right)^2 + \left(Q_{b,t}^{TG}\right)^2 \leq \left(SS^{rat}\right)^2, \quad (33a)$$

$$1.0y_{b,t}^{TG} \geq v_{b,t} \geq 1.0y_{b,t}^{TG}, \quad (33b)$$

$$60y_{b,t}^{TG} \geq f_{b,t} \geq 60y_{b,t}^{TG} \quad (33c)$$

IV. HOLISTIC FORMULATION OF BLACKSTART AND LOAD RESTORATION PROCESS WITH SYNCHRONIZATION

In this section, we formulate an optimization problem for bottom-up blackstart and load restoration of the DS leveraging DERs. Our approach involves utilizing multiple BES-based GFMI for blackstart and extending the cranking paths according to the DS switching structure to energize GFLIs while maximizing the cold load pickup without violating capacity and frequency security limits. Furthermore, we synchronize the MGs to support each other and later with the TG upon its recovery, ensuring continuous operation beyond the studied restoration horizon. Our objective is to model the complete restoration process and determine the sequence of energizing and synchronizing switching decisions for a given TG recovery instant.

A. Dynamic Radiality Constraint Driven Synchronization

Radiality constraint must be maintained at every switching sequence while blackstarting the DS. In [29], radiality constraint is developed for static case, where the network size and number of root buses are fixed. However, in the black-starting problem, the radiality constraint has to be satisfied adapting to activation status of the buses and lines. A bus with an active grid-forming source (e.g., GFMI and TG) can be considered a root bus. The number of active root bus defines the number of MGs that can be formed while maintaining the tree or radial structure. Hence, the dynamic radiality constraints are defined as:

$$\sum_{(i,j) \in \mathcal{L}} y_{ij,t}^L = \sum_{b \in \mathcal{B}} y_{b,t}^B + \sum_{b \in \mathcal{B}^{TG}} y_{b,t}^{TG} - R_t \quad (34a)$$

$$R_t = \sum_{b \in \mathcal{R}} y_{b,t}^{ES} + \sum_{b \in \mathcal{B}^{TG}} y_{b,t}^{TG} \quad (34b)$$

$$y_{b,t}^{ES} \leq y_{b,t-1}^{ES} \quad \forall b \in \mathcal{R} \quad (34c)$$

In (34a), the activation status of substation bus ($y_{b,t}^{TG}$) and other buses ($y_{b,t}^B$) have been considered separately because $y_{b,t}^{TG}$ is an input parameter to simulate various outage duration of TG, whereas $y_{b,t}^B$ are part of decision variables. Furthermore, R_t is also the decision variable defining the number of root buses in (34b). We allow GFMI buses to be non-root buses but do not permit them to become root buses again, by defining (34c). Although this formulation decide the optimal number of MGs along the black-starting and load restoration process, it is essential to coordinate frequency perturbation decisions ($\Delta f_{b,t}^*$) in GFMI, to match frequencies. This is achieved by activating $\delta_{b,t}$ at synchronizing instant, by defining a constraint as:

$$y_{b,\tau}^{ES} = 1 - \sum_{t \in [t_o, \tau]} \delta_{b,t} \quad \forall \tau \in \mathcal{T}, \forall b \in \mathcal{R} \quad (35)$$

Constraint (35) signifies that whenever a GFMI at bus b change its status from root to non-root bus, $\delta_{b,t}$ set to 1, otherwise 0.

Here, t_o is start time of balckstart and \mathcal{T} is the time horizon of study.

The dynamic radiality constraint binds the expansion of dynamic MGs in radial manner, favors synchronization by allowing them to adjust their reference frequency, and maintains radiality even after their interconnection. This is a key contribution of the paper.

B. Optimization Model

We propose a mixed-integer model for black start and load restoration planning where the primary decision variables are root bus status of GFMI ($y_{b,t}^B$, $b \in \mathcal{R}$, $t \in \mathcal{T}$), ESW/SSWs' statuses ($y_{ij,t}^L$, $(i,j) \in \mathcal{L}^{ESW} \cup \mathcal{L}^{SSW}$, $t \in \mathcal{T}$), bus blocks' statuses ($y_{m,t}^{BB}$, $m \in \mathcal{M}$), and status of switchable loads ($y_{b,t}^{NL}$, $b \in \mathcal{B}^{NL}$, $t \in \mathcal{T}$). Other decision variables pertaining to the activation of PVs, non-switchable loads, lines, and buses are associated with the bus block's status ($y_{m,t}^{BB}$). For convenience, we associate all the decision variables into vector \mathbf{x} as $\mathbf{x} = [y_{b,t}^B, y_{ij,t}^L, y_{m,t}^{BB}, y_{b,t}^{NL}]^T$.

1) *Objective Function*: The objective is to maximize the load restoration throughout the black start process. Hence, the objective is formulated as:

$$\max_{\mathbf{x}} \sum_{t \in \mathcal{T}} \sum_{b \in \mathcal{B}^{NL} \cup \mathcal{B}^{CL}} P_{b,t}^D \Delta t. \quad (36)$$

2) *Associated Constraints*: All the constraints pertaining to individual resources and networks defined in (1) to (35) are imposed on the optimization model.

3) *Model Initialization*: All GFMI are self-started, considering them to be the root buses with full SoC. Statuses of all bus blocks and switches are considered inactive. We define these initial conditions as:

$$y_{b,t \rightarrow 0}^{ES} = 1, \quad y_{i,t \rightarrow 0}^B = 1, \quad SoC_{b,t \rightarrow 0} = 1 \quad \forall i \in \mathcal{R} \quad (37a)$$

$$y_{m,t \rightarrow 0}^{BB} = 0 \quad \forall m \in \mathcal{B} \quad (37b)$$

$$y_{ij,t \rightarrow 0}^L = 0 \quad \forall (i,j) \in \mathcal{L}^{ESW} \cup \mathcal{L}^{SSW} \quad (37c)$$

4) *Nature of the Problem*: The objective function (36) is linear, and most constraints are also linear, with a few exceptions, such as the quadratic constraints (5) and (33a). Therefore, the overall formulation is a Mixed-Integer Linear Problem (MILP) with a few quadratic constraints. Such problems can be solved to optimality using off-the-shelf solvers like Gurobi or CPLEX.

C. Modeling Different Synchronizing Settings

The black start and load restoration problem has traditionally been examined without considering the impact of synchronizing switching and generally ends up with the restoration forming multiple islands. Synchronization with the TG is essential to ensure the continuity of service beyond the study period (\mathcal{T}). The above problem can be modeled in two different synchronizing settings, as shown in Fig. 8.

1) *Optimal Switching for Energizing and Synchronizing*: This is our proposed setting, where we consider a number of root bus (R_t) as an optimization variable having lower and

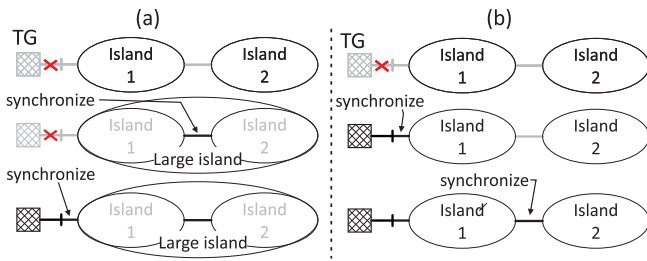


Fig. 8. Synchronizing settings: (a) optimally synchronizing the islands while black starting to form a large island, which is later synchronized with TG; (b) synchronizing islands one after another with TG after TG is available.

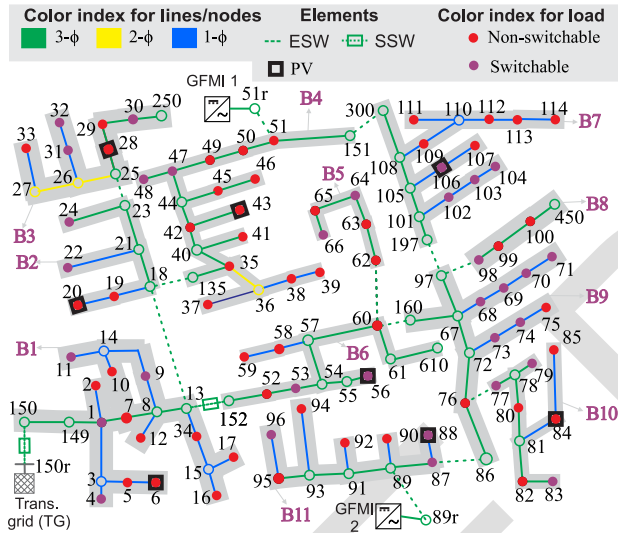


Fig. 9. Modified IEEE 123 bus test distribution system.

TABLE II
LOCATION OF SSWs AND GFMI IN IEEE-123-BUS TEST SYSTEM

Case studies	Location :capacity (bus : MVA/ MWh)	SSW locations
2 GFMI	51r : 2.45/4.6 89r : 2.65/3.42	(150r, 150) , (13, 152)
4 GFMI	51r : 1.35/2.5 89r : 1.5/2.35 29r : 0.95/1.17 152r : 1.3/2.0	(150r, 150) , (18, 135), (13, 18), (60, 160), (97, 197)

TABLE III
VSG-BASED GFMI PARAMETERS [20]

Parameters	values in pu
(H, D, K^f, γ)	(4.1, 89, 0.093)

upper bounds of 1 and $|\mathcal{R} + \mathcal{B}_{ss}|$, respectively. Furthermore, both the energizing and synchronizing switching are optimally decided while black starting.

2) *Switching for Synchronizing After TG is Available*: In this setting, a number of root buses (R_r) are fixed to the number of GFMI, and only energizing switching is optimized. After a TG is available, it is reduced progressively step by step with a pre-defined reconnecting rule. A general rule is to synchronize the island near the TG at first and then keep on synchronizing its neighboring island until all the islands are connected to the grid, as shown in Fig. 8b.

V. RESULTS

To analyze the performance of the proposed blackstart and load restoration framework, we employed the IEEE-123-bus test DS, which is an unbalanced network having a maximum load demand of 3.49 MW. As shown in Fig. 9, we segmented the entire network into 11 bus-blocks (B1 to B11) interconnected by either a ESW or SSW. All the switches are considered to be 3- ϕ . Furthermore, 1- ϕ /3- ϕ PVs are allocated throughout the network, with locations indicated by square-shaped boxes. A total of 965 kW of PVs are installed in this test system, which accounts for about 28% of the maximum demand. Reactive power from PV inverters is assumed controllable while complying with IEEE 1547 standards. To represent a realistic situation, we assumed that 60% of point loads are non-switchable (hard-wired) and the remaining 40% are switchable. Their locations are shown by red and purple circles in Fig. 9. We will conduct case studies to demonstrate the advantages of the proposed framework, considering scenarios with two and four BES-based GFMI. Locations and power/energy capacity of BES-based GFMI for both the case studies are listed in Table II. In both case studies, the aggregate power and energy capacity of the GFMI are identical. Their total effective capacity (i.e., state of charge between 1 and 0.2) is sufficient to sustain all non-switchable loads for only three hours. Additionally, the locations of SSWs are shown in Table II, while all other switches are ESWs.

Firstly, we will verify the accuracy of the estimated frequency responses of GFMI using an RMS model of the DS in DigSILENT PowerFactory. The parameters for all GFMI have been considered identical and their values in Table III represent the behavior of realistic synchronous generator, adopted from [20]. Secondly, considering only two GFMI, we will analyze, evaluate, and benchmark the performance of the proposed framework under various scenarios of TG restoration following an extended blackout. Lastly, we will summarize the performance of the proposed framework with four GFMI.

A. Verification of Frequency Responses of GFMI

We built a distribution network with virtual-synchronous-generator-based GFMI model in the DigSILENT PowerFactory and executed RMS simulation with load pickup events to evaluate the accuracy of estimated frequency responses listed in (2), (7), and (8). The transient responses of the GFMI are recorded for 1, 2, and 10 MW load pickups, as shown in Fig. 10. This dynamic simulation provided actual values of f^{qss} , $RoCoF$, and f^{nad} , which are used as references to evaluate the accuracy of the estimations, as shown in Table IV. The accuracy of the estimated frequency responses is above 92%, which is commendable as they only utilize initial and final QSS points. This method is more favorable for large-scale planning problem as they eliminate the requirement of assistance from the complex dynamic simulation, proposed in [14].

B. Blackstart and Load Restoration With Two GFMI

We will study the proposed framework under two synchronization settings, illustrated in Section IV-C, for a scenario

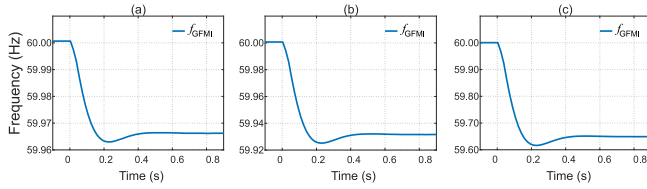


Fig. 10. Transient frequency response of the GFMI under different pick-up loads. (a) 1 MW load pickup. (b) 2 MW load pickup. (c) 10 MW load pickup.

TABLE IV
VALIDATION OF ESTIMATED FREQUENCY RESPONSES

Pick-up load (MW)	1	2	10
Measured $RoCoF$ (Hz/s)	-0.3529	-0.7058	-3.6106
Estimated $RoCoF$ (Hz/s)	-0.3780	-0.7500	-3.7500
Accuracy of $RoCoF$ (%)	92.89	93.74	96.14
Measured f^{nad} (Hz)	59.9629	59.9251	59.6161
Estimated f^{nad} (Hz)	59.9635	59.9272	59.6357
Accuracy of f^{nad} (%)	98.38	97.20	94.89
Measured f^{qss} (Hz)	59.9662	59.9316	59.6490
Estimated f^{qss} (Hz)	59.9666	59.9333	59.6666
Accuracy of f^{qss} (%)	98.82	97.51	94.99

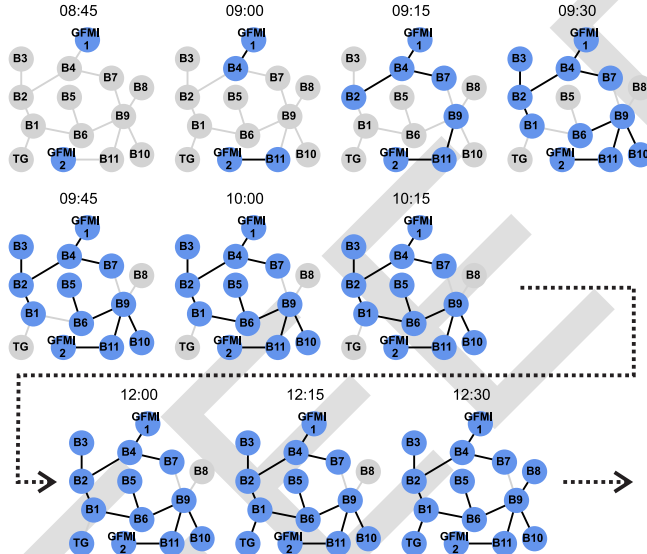


Fig. 11. Evolution of cranking paths in the proposed method.

where a blackstart is initiated at 8:45 and the TG comes online at 12:00. Furthermore, we will compare restoration metrics for other restoration instants of TG.

1) *Proposed Method – Optimized Energizing and Synchronizing Decisions:* In the proposed method, we optimize both energizing and synchronizing decisions to enhance the performance of blackstart and load restoration. The optimal sequence of establishing cranking paths obtained by the proposed method is shown in Fig. 11. Here, the blackstart initiates from two GFMI units at buses 51r and 89r at 8:45. Subsequently, the bus-blocks B4 and B11 are energized simultaneously by closing switches adjacent to GFMI units, leading to formation of two islanded MGs. Furthermore at 9:15, bus-blocks B2 and B7 are energized in the first MG, while only B9 is energized in the second MG. The boundary of these two MGs expands progressively at each time step while picking

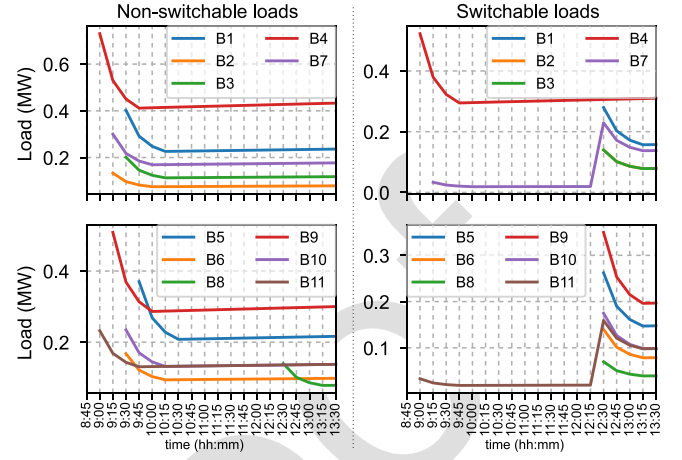


Fig. 12. Restoration of loads in the proposed method.

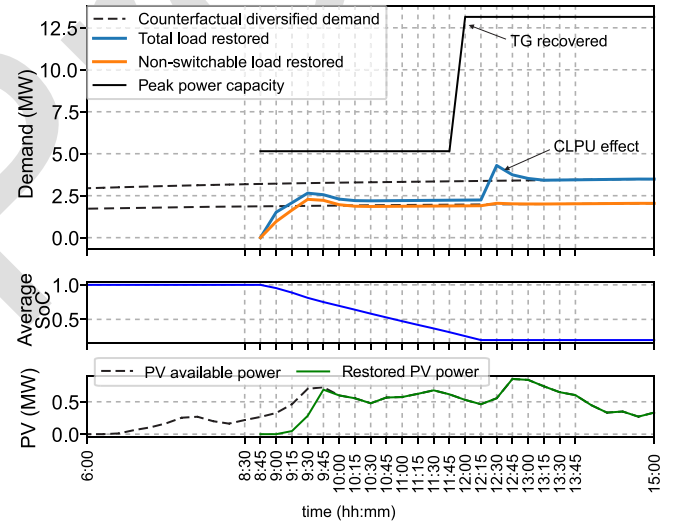


Fig. 13. Performance of blackstart and load restoration in the proposed method.

up loads and energizing PVs associated with the bus-blocks till 9:45. Note that at 9:45, only B5 is energized while B8 is not, due to the insufficient energy capacity of GFMI2. At 10:00, two MGs are synchronized and connected by closing a SSW between B1 and B6. The distribution system remains in this configuration till the TG comes online at 12:00. At 12:15, the entire network is synchronized with TG, and B8 is picked up at 12:30. This is the final configuration at which DS is operated after the successful blackstart. Note that when the bus-blocks are energized, all non-switchable loads are picked up at the same instant, as seen in Fig. 12. Depending upon the energy and power capacity of GFMI units, only few switchable loads are picked up when bus-blocks are energized. Many switchable loads are restored only after connecting with the TG, as shown in Fig. 12. Note that the system experienced higher demand at the instant of load pickup, which decayed approximately in an exponential manner due to the CLPU effect.

Fig. 13 illustrates the system restoration performance of the proposed method. The amount of restored loads increases

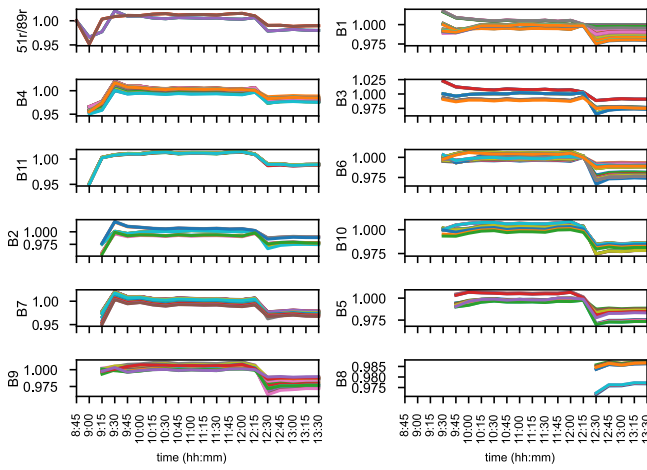


Fig. 14. Nodal voltage magnitudes at bus-blocks in the proposed method.

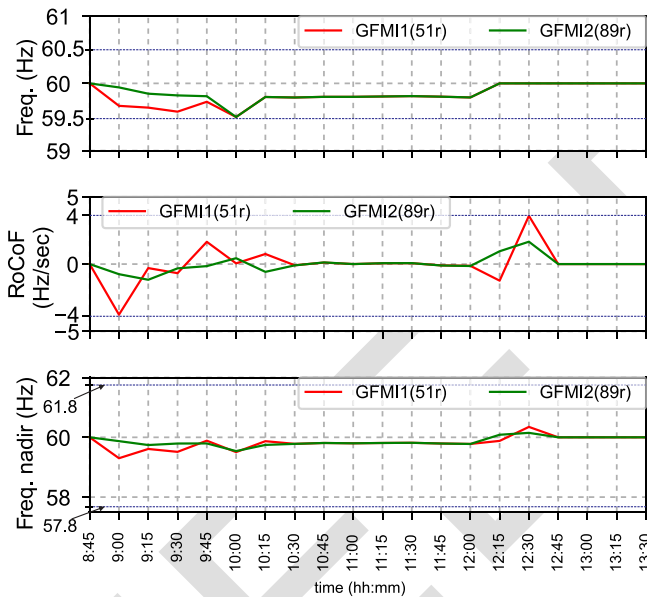


Fig. 15. Frequency constraints of GFMI1 and GFMI2 in the proposed method.

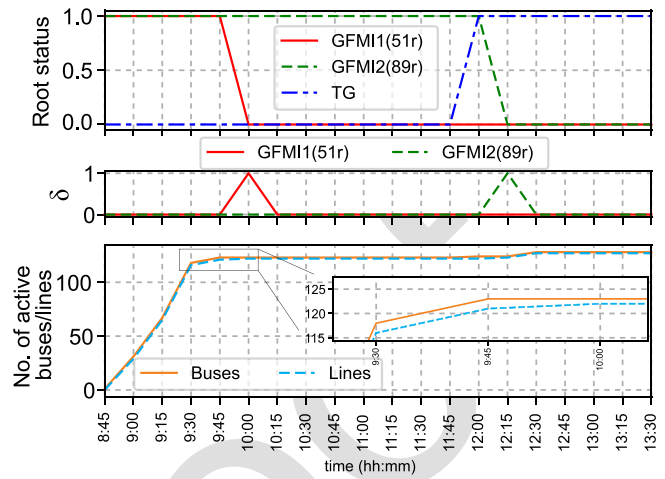


Fig. 16. Illustrating the connection between dynamic radiality constraint and synchronization.

as loads are picked up, their frequencies drop independently due to drooping characteristics until synchronization occurs at 10:00. After synchronization, the GFMI1 maintains the same QSS frequencies. At 12:15, both GFMI1 and GFMI2 synchronize with the TG and return to operating at 60 Hz. The metrics $RoCoF$ and f^{nad} are used to characterize the transient behavior of GFMI1 and GFMI2. Both metrics are within secure limits, ensuring system stability, as shown in Fig. 15.

a) *Role of dynamic radiality constraints on synchronization:* To establish a MG, a designated root bus is required to comply with radiality constraints [29]. This root bus can be supported either by a GFMI or by the TG. However, when MGs interconnect or connect with the TG, dynamically maintaining the root bus status of GFMI1 and GFMI2 becomes essential. This is managed through the dynamic radiality constraint (34a).

As shown in Fig. 16, GFMI1 and GFMI2 maintained root status, forming two isolated MGs from the start of the blackstart process at 8:45 until 9:45. At 10:00, GFMI1 dropped its root status to facilitate the interconnection of these isolated MGs, which activated a binary variable δ due to constraint (35). This δ allows the GFMI1 and GFMI2 to synchronize their frequencies according to (12). The system then operated as a single large MG until 12:00, when the TG was restored. At this point, GFMI2 dropped its root status and activated δ , helping to synchronize GFMI1 and GFMI2's frequencies with TG. Throughout the blackstart and load restoration process, the difference between the number of active buses and lines consistently equaled the number of root buses. For example, before 10:00, there were two root buses, whereas, between 10:00 and 12:00, only one root bus was active. One can observe that the difference in the number of active buses and lines reduced from 2 to 1 after the synchronization of MGs at 10:00 in the zoomed portion of Fig. 16. This also happened in the second synchronization at 12:15.

2) *Benchmark Method – Optimal Energizing Decisions and Rule-Based Synchronization:* Existing research on blackstart and load restoration using DERs often neglects synchronization considerations. As a result, these approaches typically lead to the formation of multiple islanded MGs, raising concerns

with each switching decision after the blackstart process. Non-switchable loads are quickly restored due to their hard-wired connections, as they are integral to forming cranking paths for energizing grid-following PVs. In contrast, the restoration of switchable loads is deferred to prioritize the expansion of cranking paths and the integration of additional PVs, thereby enhancing the overall restoration process. Consequently, most switchable loads are restored only after the connection with the TG, as shown in Fig. 13. The aggregated PV generation also increases, as more PVs come online with the expansion of cranking paths. The SoC curve demonstrates that the energy capacities of both GFMI1 and GFMI2 are fully utilized during the blackstart and load restoration phases, prior to the TG coming online. Throughout this process, the voltage at each node is maintained within the range of 0.95 to 1.05 pu, as shown in Fig. 14, ensuring stable and reliable operation.

All the frequency constraints for GFMI1 and GFMI2 are within an acceptable range, as shown in Fig. 15. At the initiation of the blackstart at 8:45, both GFMI1 and GFMI2 operate at 60 Hz. However,

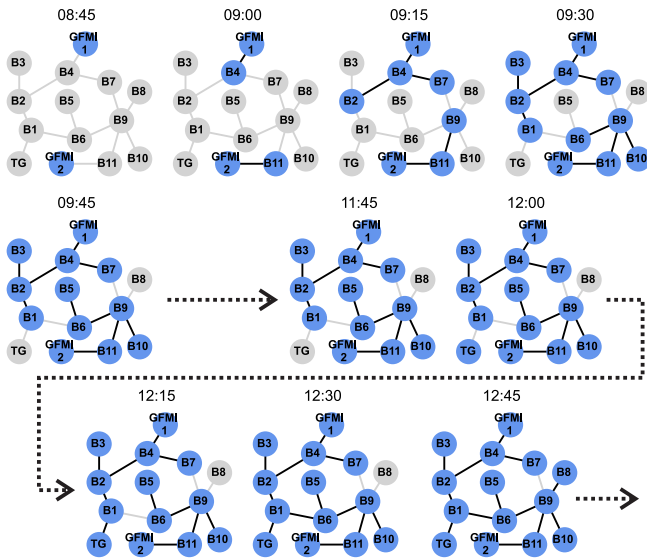


Fig. 17. Evolution of cranking paths in the benchmark method.

862 about their sustainability given the limited energy capacity
 863 of blackstart units such as BES-based GFMI. To provide a
 864 fair comparison with the proposed method, we incorporate
 865 rule-based synchronization (as outlined in Section IV-C) to
 866 merge all islanded MGs once the TG becomes available after
 867 an extended blackout. In this benchmark approach, only the
 868 ESWs are optimized, while the SSWs are operated in a
 869 predetermined sequence.

870 The evolution of cranking paths using the benchmark
 871 method is shown in Fig. 17. Unlike the proposed method,
 872 the two islanded MGs remain unsynchronized and operate
 873 independently until the TG becomes available at 12:00. At
 874 12:15, the MG located near the TG is synchronized, followed
 875 by the synchronization of the second MG at 12:30. Finally,
 876 the bus-block B8 is energized at 12:45. This configuration
 877 of the distribution system is maintained for subsequent oper-
 878 ations after a successful blackstart. The detailed results of
 879 the benchmark method are not emphasized, as they closely
 880 corroborate with those of the proposed method. However,
 881 the frequency plot, which exhibits significant differences, is
 882 explicitly presented in Fig. 18. In this method, the two GFMI
 883 operate at distinct frequencies until their synchronization with
 884 the TG—one at 12:15 and the other at 12:30. Despite these
 885 differences, the method ensures that both $RoCoF$ and f^{nad}
 886 remain within secure limits throughout the process.

887 3) *Comparison Between Proposed and Benchmark*
 888 *Methods:* Depending on the severity of the outage, the TG
 889 may have varying restoration times. Therefore, we evaluated
 890 the performance of the proposed and benchmark methods
 891 for different restoration instances of the TG. The restoration
 892 performance for a scenario where the TG is restored at 12:00
 893 is shown in Fig. 19. It is observed that optimizing both the
 894 ESW and SSWs not only rapidly restores the load but also
 895 enhances customer-hours served. The comparison for other
 896 restoration scenarios of the TG is provided in Table V. It
 897 is evident that the proposed method has a slight edge over
 898 the benchmark method in terms of restoration metrics for
 899 longer-duration outages. Next, we will examine another case

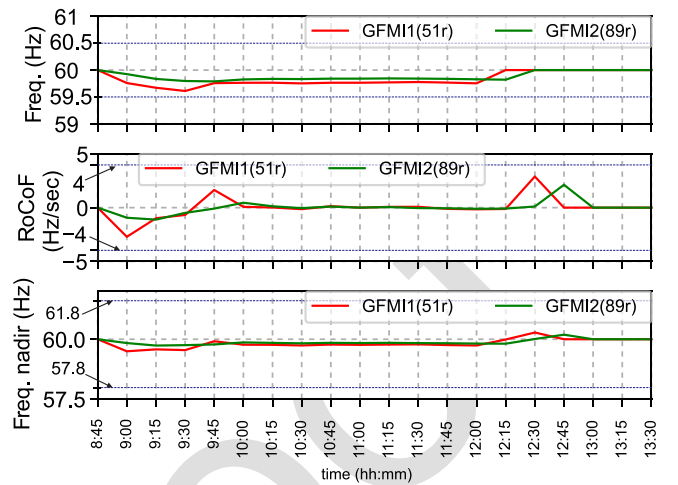


Fig. 18. Frequency constraints of GFMI in the benchmark method.

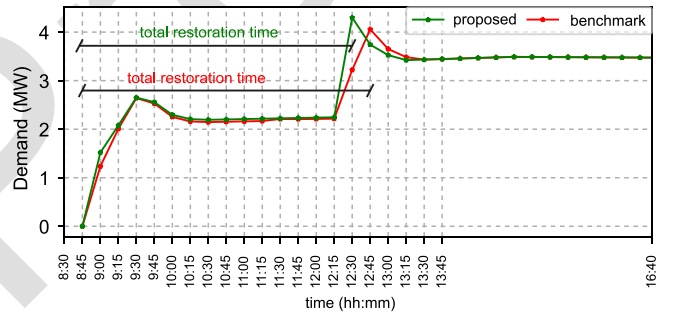


Fig. 19. Comparison of restoration metrics for 2 GFMI case.

TABLE V
 PROPOSED VS. BENCHMARK METHODS: 2-GFMI CASE

TG re- stored at	Customer hours restored (MWh)		% im- proved	DS restoration time (min)		im- proved (mins)
	proposed	benchmark		proposed	benchmark	
10:00	26.99	26.93	0.22	105	105	0
11:00	26.25	25.95	1.16	165	180	15
12:00	23.67	23.33	1.46	225	240	15
13:00	21.11	20.74	1.78	285	300	15
14:00	18.05	17.61	2.5	345	360	15

study involving four GFMI to highlight the significance of
 the proposed method.

C. Blackstart and Load Restoration With Four GFMI

For this case study, we connected an additional two GFMI
 at buses 29 and 152 in the IEEE-123-bus test system, as
 shown in Fig. 9. The allocated power and energy capacities
 are detailed in Table II. With four GFMI, four MGs will
 be formed, necessitating more SSWs. The new allocation of
 SSWs is also shown in Table II. We examined the performance
 of the proposed and benchmark methods for the modified test
 system, keeping the loads and PV generation profile the same
 as in the previous case study. The summary of the simulation
 results are shown in Table VI. It is observed that there is
 a significant improvement in the customer hours restoration

TABLE VI
 PROPOSED VS. BENCHMARK METHODS: 4-GFMIS CASE

TG re- stored at	Customer hours restored (MWh)		% im- proved	DS restoration time (min)		impr- oved (mins)
	proposed	benchmark		proposed	benchmark	
10:00	27.86	26.57	4.86	105	135	30
11:00	26.59	25.28	5.18	165	195	30
12:00	23.96	22.64	5.83	225	270	45
13:00	21.35	19.54	9.26	285	330	45
14:00	18.29	16.41	11.46	345	390	45

metric for longer outages (e.g., 11.46% for TG coming online at 14:00), while the restoration time is reduced by 45 minutes.

VI. CONCLUSION

This paper proposes a comprehensive bottom-up framework for blackstart and load restoration planning, tailored for BES-based GFMI and renewable GFLI. The framework initiates blackstart using multiple GFMI, sequentially expands microgrid boundaries to pick up cold loads, establishes cranking paths to GFLI, synchronizes MGs to form larger islands, and ultimately synchronizes with the TG to complete the restoration process. Integration of these steps with the linearized power flow model of the DS forms the core contribution of the paper. Furthermore, we enhance GFMI models by incorporating control features from virtual synchronous generators to establish and validate quasi-steady-state and dynamic frequency responses, including ROCOF and frequency nadir. The proposed framework is validated and benchmarked on the IEEE-123-bus test system, considering configurations with two and four GFMI across various scenarios of TG recovery times. Our findings indicate that optimizing synchronization decisions facilitates faster restoration and enhances customer hours restoration during prolonged outages, particularly with increased numbers of GFMI.

The paper focuses on formulating the fundamental concepts necessary to enable and optimize synchronizing decisions during the blackstart and restoration process. We acknowledge that predicting DER generation, loads, and the timing of TG restoration involves uncertainties, which are not addressed in this paper. We plan to explore this aspect in future research.

APPENDIX A

TERMINAL VOLTAGE OF GFMI CONSIDERING VOLTAGE DROOP

Terminal voltage of GFMI deviates from the reference value (V^*) with reactive power output (Q) and voltage droop gain (K^v), which is define as:

$$|V| = V^* - K^v Q \quad (38)$$

To comply with the branch-flow model, we define the terminal voltage of GFMI in terms of $v = |V|^2$, as:

$$v = (V^* - K^v Q)^2 = (V^*)^2 - 2V^* K^v Q + (K^v Q)^2. \quad (39)$$

In the square form, the deviation from $(V^*)^2$ is non-linear with Q . Hence, we simplify (39) by defining a new variable Δv^{cc} , which represents the last two terms in (39). With this, the terminal voltage is written as:

$$v = (V^*)^2 + \Delta v^{cc} \quad (40)$$

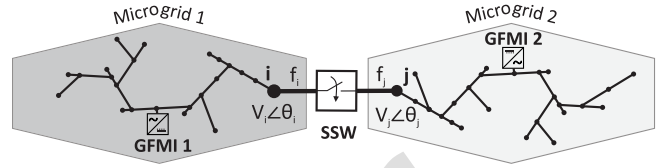


Fig. 20. Two microgrid interconnected with SSW.

APPENDIX B

CALCULATION OF γ TO ESTIMATE f^{nad} FOR A VSG

The calculation of γ is based on VSG control in Fig. 3a and work presented for the synchronous generator in [21], and is expressed as:

$$\gamma_i = \alpha_i \sqrt{1 - \xi_i^2} e^{-\xi_i \omega_i^o t_i^{nad}} \quad (41)$$

$$\text{where, } \alpha_i = \sqrt{\frac{T_i K_i^f}{2H_i}}, \quad \omega_i^o = \frac{D_i + K_i^f}{2H_i T_i}, \quad \xi_i = \frac{2H_i + D_i T_i}{2(D_i + K_i^f)} \omega_i^o$$

$$t_i^{nad} = \frac{1}{\omega_i^r} \tan^{-1} \left(\frac{\omega_i^r T_i}{\xi_i \omega_i^o T_i - 1} \right), \quad \omega_i^r = \omega_i^o \sqrt{1 - \xi_i^2}$$

Although calculation of γ_i is highly non-linear, it is a constant parameter and do not increase the complexity of the proposed blackstart optimization problem.

APPENDIX C

MCCORMICK RELAXATIONS OF BILINEAR CONSTRAINTS

McCormick relaxation transforms the non-convex bilinear constraint into a set of linear constraints. For illustration, consider a bilinear constraint $f(\mathbf{x})$ defined as:

$$f(\mathbf{x}) = \sum_{(i,j) \in BL} x_i x_j + g(\mathbf{x}). \quad (42)$$

Here, $\mathbf{x} = [x_1, \dots, x_n]^T$, BL is an (i, j) index set that defines the bilinear terms $x_i x_j$, and $g(\mathbf{x})$ is a linear function. By replacing $x_i x_j = w_{ij}$ and introducing additional linear inequalities, the above constraint can be relaxed as:

$$f(\mathbf{x}) = \sum_{(i,j) \in BL} w_{ij} + g(\mathbf{x}) \quad (43a)$$

$$w_{ij} \geq [x_i] x_j + x_i [x_j] - [x_i] [x_j] \quad (43b)$$

$$w_{ij} \geq [x_i] x_j + x_i [x_j] - [x_i] [x_j] \quad (43c)$$

$$w_{ij} \leq [x_i] x_j + x_i [x_j] - [x_i] [x_j] \quad (43d)$$

$$w_{ij} \leq x_i [x_j] + [x_i] x_j - [x_i] [x_j] \quad (43e)$$

$$[x] \leq \mathbf{x} \leq [x] \quad (43f)$$

Here, $[x]$ and $[x]$ are lower and upper bounds of \mathbf{x} . Note that McCormick relaxations also holds true with binary/integer variables.

APPENDIX D

SYNCHRONIZING CRITERIA FOR CLOSING SSW

Let's consider two MGs connected by a SSW across buses i and j , as shown in Fig. 20, to elucidate the synchronizing criteria. A well-perceived set of synchronizing criteria to interconnect these MGs is described in [30], as:

$$V_i = V_j, \theta_i = \theta_j, \quad (44a)$$

$$\text{and } f_i = f_j. \quad (44b)$$

Once this condition is met, the power flow across the SSW will be virtually zero, even when the switch is closed.

This condition is released once synchronization is successful, allowing the power flow across the switch to resume as desired.

The power flow ($P_{ij} + jQ_{ij}$) across the SSW (i, j) is given by:

$$P_{ij} + jQ_{ij} = (V_i \angle \theta_i - V_j \angle \theta_j)^2 / Z_{ij}, \quad (45)$$

where Z_{ij} is the impedance of the switch. Using this relationship, we can enforce condition (44a) by ensuring that P_{ij} and Q_{ij} to be virtually zero, expressed as:

$$-\epsilon \leq P_{ij} \leq \epsilon \text{ and } -\epsilon \leq Q_{ij} \leq \epsilon \quad (46)$$

Therefore, condition (46) can be effectively applied in the branch flow model, along with condition (44b) imposed for GFMs. Importantly, the synchronization condition (46) only needs to be applied during the synchronization period and should be removed thereafter.

ACKNOWLEDGMENT

The views expressed in the article do not necessarily represent the views of the DOE or the U.S. Government. The U.S. Government retains and the publisher, by accepting this article for publication, acknowledges that the U.S. Government retains a non-exclusive, paid-up, irrevocable, worldwide license to publish or reproduce the published form of this work or allow others to do so, for U.S. Government purposes.

REFERENCES

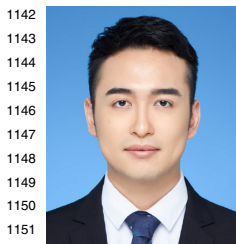
- [1] Z. Wang and J. Wang, "Self-healing resilient distribution systems based on sectionalization into microgrids," *IEEE Trans. Power Syst.*, vol. 30, no. 6, pp. 3139–3149, Nov. 2015.
- [2] Z. Wang, B. Chen, J. Wang, and C. Chen, "Networked microgrids for self-healing power systems," *IEEE Trans. Smart Grid*, vol. 7, no. 1, pp. 310–319, Jan. 2016.
- [3] (Am. Public Power Assoc., Washington, DC, USA). *Restoration Best Practices Guidebook*. 2018. [Online]. Available: <https://www.publicpower.org/resource/restoration-best-practices-guidebook#:text=The>
- [4] J. Li, X.-Y. Ma, C.-C. Liu, and K. P. Schneider, "Distribution system restoration with microgrids using spanning tree search," *IEEE Trans. Power Syst.*, vol. 29, no. 6, pp. 3021–3029, Nov. 2014.
- [5] A. Sharma, D. Srinivasan, and A. Trivedi, "A decentralized multiagent system approach for service restoration using DG islanding," *IEEE Trans. Smart Grid*, vol. 6, no. 6, pp. 2784–2793, Nov. 2015.
- [6] Y. Wang et al., "Coordinating multiple sources for service restoration to enhance resilience of distribution systems," *IEEE Trans. Smart Grid*, vol. 10, no. 5, pp. 5781–5793, Sep. 2019.
- [7] B. Chen, C. Chen, J. Wang, and K. L. Butler-Purry, "Sequential service restoration for unbalanced distribution systems and microgrids," *IEEE Trans. Power Syst.*, vol. 33, no. 2, pp. 1507–1520, Mar. 2018.
- [8] T. Ding, Z. Wang, M. Qu, Z. Wang, and M. Shahidehpour, "A sequential black-start restoration model for resilient active distribution networks," *IEEE Trans. Power Syst.*, vol. 37, no. 4, pp. 3133–3136, Jul. 2022.
- [9] W. Liu and F. Ding, "Collaborative distribution system restoration planning and real-time dispatch considering behind-the-meter DERS," *IEEE Trans. Power Syst.*, vol. 36, no. 4, pp. 3629–3644, Jul. 2021.
- [10] A. Arif, B. Cui, and Z. Wang, "Switching device-cognizant sequential distribution system restoration," *IEEE Trans. Power Syst.*, vol. 37, no. 1, pp. 317–329, Jan. 2022.
- [11] B. Chen, Z. Ye, C. Chen, and J. Wang, "Toward a MILP modeling framework for distribution system restoration," *IEEE Trans. Power Syst.*, vol. 34, no. 3, pp. 1749–1760, May 2019.
- [12] X. Gao, R. R. Nejad, and W. Sun, "Decentralized distribution system restoration with grid-forming/following inverter-based resources," in *Proc. IEEE Power Energy Soc. Gener. Meeting*, Jul. 2022, pp. 1–5.
- [13] L. Che and M. Shahidehpour, "Adaptive formation of microgrids with mobile emergency resources for critical service restoration in extreme conditions," *IEEE Trans. Power Syst.*, vol. 34, no. 1, pp. 742–753, Jan. 2019.
- [14] Q. Zhang, Z. Ma, Y. Zhu, and Z. Wang, "A two-level simulation-assisted sequential distribution system restoration model with frequency dynamics constraints," *IEEE Trans. Smart Grid*, vol. 12, no. 5, pp. 3835–3846, Sep. 2021.
- [15] Y. Du, H. Tu, X. Lu, J. Wang, and S. Lukic, "Black-start and service restoration in resilient distribution systems with dynamic microgrids," *IEEE J. Emerg. Select. Topics Power Electron.*, vol. 10, no. 4, pp. 3975–3986, Aug. 2022.
- [16] F. Liu, C. Chen, C. Lin, G. Li, H. Xie, and Z. Bie, "Utilizing aggregated distributed renewable energy sources with control coordination for resilient distribution system restoration," *IEEE Trans. Sustain. Energy*, vol. 14, no. 2, pp. 1043–1056, Apr. 2023.
- [17] J. L. Domínguez-García, A. Pepicciello, P. Paradell, and A. Ivanova (IEEE Smart Grid Bull., Piscataway, NJ, USA). *Dynamic Microgrids for Strengthening Power System Resilience*. Apr. 2023. [Online]. Available: <https://smartgrid.ieee.org/bulletins/april-2023/dynamic-microgrids-for-strengthening-power-system-resilience>
- [18] (North Am. Elect. Reliabil. Corp., Atlanta, GA, USA). *Standard PRC-024-2—Generator Frequency and Voltage Protective Relay Settings*. 2021. [Online]. Available: <https://www.nerc.com/pa/Stand/Reliability>
- [19] (Am. Public Power Assoc., Washington, DC, USA). *Restoration Best Practices Guidebook*. Jun. 2018. [Online]. Available: <https://www.publicpower.org/resource/restoration-best-practices-guidebook#:text=The%20Restoration%20Best%20Practices%20Guidebook,restoration%20operations%20and%20emergency%20management>
- [20] M. N. Ambia, K. Meng, W. Xiao, A. Al-Durra, and Z. Y. Dong, "Interactive grid synchronization-based virtual synchronous generator control scheme on weak grid integration," *IEEE Trans. Smart Grid*, vol. 13, no. 5, pp. 4057–4071, Sep. 2022.
- [21] L. Liu, Z. Hu, Y. Wen, and Y. Ma, "Modeling of frequency security constraints and quantification of frequency control reserve capacities for unit commitment," *IEEE Trans. Power Syst.*, vol. 39, no. 1, pp. 2080–2092, Jan. 2024.
- [22] T. Kim et al., "Voltage balancing capability of grid-forming inverters," *IEEE Open Access J. Power Energy*, vol. 9, pp. 479–488, 2022.
- [23] D. B. Rathnayake, R. Razzaghi, and B. Bahrani, "Generalized virtual synchronous generator control design for renewable power systems," *IEEE Trans. Sustain. Energy*, vol. 13, no. 2, pp. 1021–1036, Apr. 2022.
- [24] C.-T. Lee, R.-P. Jiang, and P.-T. Cheng, "A grid synchronization method for droop controlled distributed energy resources converters," in *Proc. IEEE Energy Convers. Congr. Expo.*, 2011, pp. 743–749.
- [25] P. M. Castro, "Tightening piecewise McCormick relaxations for bilinear problems," *Comput. Chem. Eng.*, vol. 72, pp. 300–311, Jan. 2015. [Online]. Available: <https://www.sciencedirect.com/science/article/pii/S0098135414001069>
- [26] S. Maharjan, A. M. Khambadkone, and J. C.-H. Peng, "Integration of centralized and local voltage control scheme in distribution network to reduce the operation of mechanically switched devices," in *Proc. IEEE Milan PowerTech*, 2019, pp. 1–6.
- [27] F. S. Gazijahani, J. Salehi, and M. Shafie-Khah, "A parallel fast-track service restoration strategy relying on sectionalized interdependent power-gas distribution systems," *IEEE Trans. Ind. Informat.*, vol. 19, no. 3, pp. 2273–2283, Mar. 2023.
- [28] R. Cheng, Z. Wang, Y. Guo, and Q. Zhang, "Online voltage control for unbalanced distribution networks using projected Newton method," *IEEE Trans. Power Syst.*, vol. 37, no. 6, pp. 4747–4760, Nov. 2022.
- [29] Y. Wang, Y. Xu, J. Li, J. He, and X. Wang, "On the radiality constraints for distribution system restoration and reconfiguration problems," *IEEE Trans. Power Syst.*, vol. 35, no. 4, pp. 3294–3296, Jul. 2020.
- [30] M. Y. Worku, M. A. Hassan, and M. A. Abido, "Power management, voltage control and grid synchronization of microgrids in real time," *Arabian J. Sci. Eng.*, vol. 46, pp. 1411–1429, Feb. 2021.



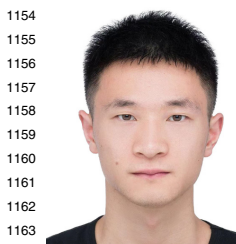
1129 **Salish Maharjan** (Member, IEEE) received the
 1130 Ph.D. degree in electrical and computer engineering
 1131 from the National University of Singapore in
 1132 2020. He is currently a Research Assistant Professor
 1133 with the Department of Electrical and Computer
 1134 Engineering, Iowa State University, Ames, IA, USA.
 1135 He was a Visiting Student with the Massachusetts
 1136 Institute of Technology, Cambridge, in 2014. His
 1137 interests include distribution system modeling, stability
 1138 analysis, and optimization and control for
 1139 techno-economic operation, and resilience enhance-
 1140 ment. He was also the recipient of the Best Paper Award at 2023 IEEE Power
 1141 & Energy General Meeting.



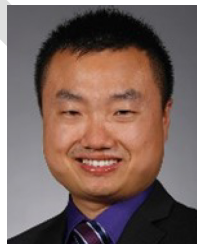
1179 **Fei Ding** (Senior Member, IEEE) received the
 1180 bachelor's and master's degrees in electrical engi-
 1181 neering from Tianjin University, China, and the
 1182 Ph.D. degree in electrical engineering from Case
 1183 Western Reserve University. She is a Distinguished
 1184 Member of Research Staff and the Manager of
 1185 Grid Automation and Controls Group, National
 1186 Renewable Energy Laboratory (NREL). She has
 1187 extensive research experience in DER grid integra-
 1188 tion, grid resilience, and distribution automation.
 1189 As PI/Co-PI, she has led over 15 research projects
 1190 funded by U.S. Department of Energy and Department of Defense ESTCP
 1191 to develop and demonstrate advanced DER technologies to enhance grid
 1192 reliability, resilience, and cybersecurity. She is a recipient of the Rising
 1193 Star Award, the Chairman's Award, and the President's Award at NREL.
 1194 She serves as an Associate Editor for the IEEE TRANSACTIONS ON
 1195 SMART GRID, the IEEE TRANSACTIONS ON POWER SYSTEMS, IEEE
 1196 POWER ENGINEERING LETTERS, and *IET Generation, Transmission, and*
 1197 *Distribution*. She is the Chair of Awards Subcommittee of IEEE PES
 1198 Power System Operation, Planning and Economics Committee, and the Vice
 1199 Chair of IEEE PES Working Group on Behind-the-Meter DERs: Estimation,
 1200 Uncertainty Quantification, and Control.



1142 **Cong Bai** (Graduate Student Member, IEEE)
 1143 received the B.S. degree in electrical engineering
 1144 and its automation from the Kunming University of
 1145 Science and Technology, Kunming, China, in 2020,
 1146 and the M.S. degree in electrical engineering from
 1147 Chongqing University, Chongqing, China, in 2023.
 1148 He is currently pursuing the Ph.D. degree with the
 1149 Department of Electrical and Computer Engineering,
 1150 Iowa State University, Ames, IA, USA. His current
 1151 research interests include power system restoration,
 1152 inverter-based resource integration, and control and
 1153 optimization of distribution systems.



1154 **Han Wang** (Member, IEEE) received the B.Sc.
 1155 degree in new energy science and engineering from
 1156 the Chinese University of Hong Kong, Shenzhen,
 1157 China, in 2019, and the Ph.D. degree in electron-
 1158 ic and electrical engineering from the University
 1159 of Leeds, Leeds, U.K., in 2023. He is currently
 1160 a Postdoctoral Research Associate with the
 1161 Department of Electrical and Computer Engineering,
 1162 Iowa State University, Ames, IA, USA. His research
 1163 interests include electric vehicle charging analy-
 1164 sis and control, electricity market, power system
 1165 resilience, artificial intelligence applications in power systems, and power
 1166 system optimization.



1201 **Zhaoyu Wang** (Senior Member, IEEE) received the
 1202 B.S. and First M.S. degrees in electrical engineer-
 1203 ing from Shanghai Jiao Tong University, and the
 1204 Second M.S. and Ph.D. degrees in electrical and
 1205 computer engineering from the Georgia Institute of
 1206 Technology. Since 2015, he has been an Assistant,
 1207 an Associate, and the Full Professor with Iowa
 1208 State University. He is the lead Principal Investigator
 1209 for over \$24M projects funded by the National
 1210 Science Foundation, the Department of Energy,
 1211 National Laboratories, PSERC, and Iowa Economic
 1212 Development Authority. His research interests include optimization and data
 1213 analytics in power distribution systems and microgrids. He was the recipient
 1214 of the National Science Foundation CAREER Award, the IEEE Power and
 1215 Energy Society Outstanding Young Engineer Award, the Northrop Grumman
 1216 Endowment, the College of Engineering's Early Achievement in Research
 1217 Award, and the Harpole-Pentair Young Faculty Award Endowment. He is the
 1218 Secretary and Technical Committee Program Chair of IEEE Power System
 1219 Operation, Planning and Economics (PSOPE) Committee, the Vice Chair
 1220 of IEEE Distribution System Operation and Planning Subcommittee, the
 1221 Secretary of IEEE Task Force on IEEE P3102 Standard for Conservation
 1222 Voltage Reduction Data Collection and Management Procedures, and the
 1223 Vice Chair of IEEE Task Force on Advances in Natural Disaster Mitigation
 1224 Methods. He is an Associate Editor of the IEEE TRANSACTIONS ON
 1225 SUSTAINABLE ENERGY, IEEE OPEN ACCESS JOURNAL OF POWER AND
 1226 ENERGY, IEEE POWER ENGINEERING LETTERS, and *IET Smart Grid*. He
 1227 was an Associate Editor of the IEEE TRANSACTIONS ON POWER SYSTEMS,
 1228 the IEEE TRANSACTIONS ON SMART GRID, and the Chair of PSOPE Awards
 1229 Subcommittee.



1167 **Yiyun Yao** (Member, IEEE) received the M.S. and
 1168 Ph.D. degrees in electrical engineering from the
 1169 Illinois Institute of Technology, Chicago, IL, USA,
 1170 in 2015 and 2019, respectively. He is currently a
 1171 Researcher with the National Renewable Energy
 1172 Laboratory, Golden, CO, USA, where he focuses on
 1173 power system resilience, distributed energy resource
 1174 integration, and optimization techniques for grid
 1175 operations. He has authored many publications in
 1176 leading IEEE journals and conferences. He is a
 1177 recipient of multiple Best Paper Awards and an
 1178 outstanding reviewer awards from IEEE.